Effect of processing temperature on film properties of ZnO by aqueous method and related organic photovoltaics and LEDs

Jiaqi Zhang[1,2,3*], Hengxiang Yang[1], Xiaoyu Zhang[1], Maurizio Morbidoni[3], Claire H. Burgess[3], Rebecca Kilmurray[3], Martyn A. McLachlan[3*]

[1] College of Materials Science and Engineering, Key Laboratory of Automobile Materials, Ministry of Education, Jilin University, Changchun, 130012, China

[2] School of Chemistry and Environmental Engineering, Changchun University of Science and Technology, Changchun, 130013, China

[3] Department of Materials and Centre for Plastic Electronics, Imperial College London, London SW7 2AZ, UK

Email: zhangjiaqi@jlu.edu.cn

Abstract

Here the influence of processing temperature on the properties of zinc oxide (ZnO) thin films fabricated using a carbon-free solution process is investigated. Our results show that the film processing temperature influences a wide range of structural and electrooptical properties. Films processed at 100 ℃ are shown to be formed of coalesced ZnO nanoparticles, the dimensions of which increase with processing temperature, accompanied by an increase in electron mobility. ZnO films processed at different temperatures were incorporated as electron transport layers (ETLs) in organic photovoltaic devices with PCDTBT:$PC_{71}BM$ as the active layer. We find that the ETLs processed at low temperature (100 - 200 °C) exhibit excellent device performance compared with those prepared at elevated temperatures, an affect we attribute to shifts in work function and electrical conductivity. Interestingly a similar trend is observed when our ZnO is used as an electron injection layer in organic light emitting diodes, where the EILs processed > 200 °C have higher turn-on voltages and lower efficiencies than those annealed in the 100-200 °C range.

Introduction

Organic electronics have seen tremendous progress since the first reports on organic photovoltaics (OPVs)[1] and organic light emitting diodes (OLEDs)[2] almost 25 years ago. This success can be ascribed to the possibility to realize low-cost, large area devices compatible with rapid solution processing routes[3–5]. However, inorganic materials are widely used in organic electronics as they enhance the stability and lifetime of devices. For example, inorganic metal oxides are commonly employed as selective charge carrier layers in OPVs and OLEDs thanks to their excellent charge transport properties, easy control of nanostructure, and doping[6–8]. Among the metal oxides used as electron transport layers, zinc oxide (ZnO) has shown tremendous promise owing to the combination of its direct band gap, high transparency in the visible range and high electron mobility[9,10].

There are a variety of methods to fabricate ZnO, including hydrothermal growth[11,12], pulsed laser deposition[13], spray pyrolysis[14], sol-gel processes[15,16] and colloidal nanoparticles[17]; among them, solution processing allows low-cost and large-area manufacturing. Sol-gel synthesis and colloidal nanoparticles are two widely used methods for the preparation of ZnO solutions. High quality ZnO thin films with low defect density have been prepared by gamma ray irradiation of a ZnO precursor solution by low temperature annealing (130 °C), an *in-situ* sol-gel conversion method[18]. UV treatments have also been used to rapidly convert precursors into ZnO and as a means of defect passivation[19]. Further modifications to the surface properties have been made by a complex variety of application specific modifications that result in changes in physical *e.g.* wettability, roughness and electronic *e.g.* work-function and electron mobility.[20]

However, in general sol-gel methods requires high-temperature annealing to completely remove organic residues and prepare pure ZnO thin films,[16] and high-temperature processing may result in inhomogeneity of the films and also places restrictions on the use of flexile (polymeric) substrates [21]. For colloidal nanoparticles, the synthesis route of dispersed ZnO nanoparticle solution is relatively complex, including long reaction durations followed by repeated precipitation, washing and dilution procedures. Moreover, ligand-linked

nanoparticles typically require high temperature annealing, while ligand-free nanoparticles usually have the suffer from poor dispersion stability[22,23].

For around a decade one aqueous processed method, using $Zn(OH)_x(NH3)_y^{(2-x)+}$ as the precursor, attracted interest owing to its simple and green strategy[24]. This method enables ZnO crystallization at low temperatures (< 150 °C) exploiting metal-ammine decomposition and hydroxide condensation/dehydration processes. Additionally, the fast, low-energy kinetics of these reactions provide superior film morphologies: low surface roughness and high film uniformity[24]. This carbon-free ZnO processing method was first reported in thin film transistors (TFTs)[24–29] while recently its use in OPV devices has been explored[30–35]. Because of the low reaction temperature of this method, the devices avoid the thermal stability issue caused by high temperature treatment[36].

There are two typical synthesis routes of ZnO formation by this carbon-free chemistry. One is a two-step process: $Zn(OH)_2$ precipitate is synthesized first and then it is solvated into aqueous ammonia to form ammine-hydroxo zinc solutions[24]. Unlike this method that requires precipitation, washing and dilution procedures to prepare precursor solution, the other is a single-step process, which involves dissolution of ZnO powders or ZnO hydrates directly into ammonia solution[26,31]. The latter is utilized in this work. Despite the attention this process has received there is little research investigating the influence of processing temperature [24,31,34]. For the single-step approach processing temperature is typically limited to values below 200 °C and the influence of higher temperatures on film properties is unclear.

Here we have conducted a range of complementary measurements to investigate the influence processing temperature from 25 – 450 °C on the structural, compositional, optical, surface morphological and electrical properties of ZnO films. The impact of the different processing temperatures on OPV performance is first studied and we show that device performances are comparable when the processing temperature is in the range of 100 – 200 °C, consistent with the existing literature[31,33,34]. However, a dramatic decrease of

OPV efficiency occurs with ZnO ETLs annealed at 450 °C. In addition, the aqueous processed ZnO films are utilized as electron injection layers for OLEDs.

Results and discussion

We carried out a range of complementary measurements on the ZnO layers beginning with an assessment of the crystallinity using X-ray diffraction (XRD). The influence of processing temperature on crystallinity is shown in **Figure 1a**. No peaks corresponding to crystalline ZnO are seen in the XRD patterns of films deposited at 100 °C. In contrast those prepared at 200 °C show clearly (100) and (101) diffraction peaks and evidence of a (002) peak developing. Further raising the temperature to 450 °C results in the development of these peaks, indicating a greater degree of crystallinity consistent with the elevated processing temperature. From these XRD data a measure of crystallite size can be made using the Scherrer method, **Table 1**. To further examine the structure of the 100 °C film we carried out high resolution transmission electron microscopy (HRTEM), **Figure 1b**. The image shows clearly the presence of nanocrystalline domains of ZnO, indexed to the Wurtzite phase of ZnO. The inset in the micrograph shows a fast Fourier transform (FFT) taken from the ZnO region of the image indicating the presence of multiple crystalline domains within the film. The combination of the nanoscale domain size and the low film thickness (420 nm) may explain the absence of peaks in the XRD characterization of the 100 °C films.

The presence of ZnO nanoparticles in the 100 °C processed films is further confirmed from optical transmission measurements. **Figure 1c** shows the transmission spectra from films prepared over the full temperature range investigated. All spectra show high transparency in the visible region, a clear absorption edge around 370 – 380 nm is observed for the thermally treated films from which the optical bandgap has been calculated by the Tauc plot, **Figure 1d**. The exceptionally high bandgap of the as-cast film (5.54 eV) likely originates from the precursor species $Zn(OH)_x(NH3)_y^{(2-x)+}$.For films annealed between 100 - 450 °C, the measured absorption edge red shifts with increasing temperature, from 367 nm (100 °C) to 382 nm (450 °C) with a corresponding reduction in optical bandgap from 3.38 eV to 3.24 eV. The enlarged bandgap of the 100 °C processed film may originate from quantum

confinement effects in this case rather than band-tailing effects seen in amorphous films. [16,37-38]

To understand the compositional evolution with changing processing temperature, we first performed Fourier transform infra-red spectroscopy (FTIR) analysis, **Figure 2a**. The as-cast film shows strong O−H stretching and N−H deformation features, indicating the presence of $Zn(OH)_x(NH3)_y^{(2-x)+}$. In contrast, the films thermally annealed at 100 – 200 °C show near identical spectra with neither the O−H or N−H features being present, confirming that decomposition and conversion of the precursor has occurred at only 100 °C. We further probed the composition of the films using X-Ray photoelectron spectroscopy (XPS). Spectra of the O1s core levels are shown in **Figure 2b-d**, with data for the C1s, N1s, Zn2p in **Supporting Figure 1**. To ensure a fair comparison among peak positions, all spectra were corrected to the ubiquitous C1s signal at 284.8 eV. The O1s spectra display two overlapping peaks, the lower binding energy peak assigned to Zn−O (oxide) peak and the higher binding energy assigned to O-H,[34], the later originating from adsorbed atmospheric moisture, dangling −O-H surface bonds and/or zinc hydroxide impurities. A systematic decrease in the intensity of the O−H, relative to the Zn−O (oxide) peak, can be observed as the temperature increases which may point to the later as being the most likely source of O-H however in contrast the N1s spectra do not show a signal for ZnO processed between 100 and 450 °C; this is in excellent agreement with the FTIR results, indicating that no zinc precursor residue remains.

The surface morphology was studied using atomic force microscopy (AFM) and scanning electron microscopy (SEM). The AFM results, **Figure 3**, show smooth film surfaces at all processing temperatures. A well-defined granular structure is observed on the surface of the films thermally annealed with temperature having little impact on the size of shape of the visible features. Subtle variations in the surface root mean square (RMS) roughness are observed as the films are heated and as the film undergoes compositional modification and structural reordering. The SEM images indicate also excellent spatial uniformity for all ZnO films, **Figure 4**. Large area images show full coverage for all films, as shown in **Supporting**

Figure 2. The as-cast film displays a 'cloud-like' morphology that is likely an artefact of the unreacted precursor and solvent present. After annealing, a granular morphology is seen for all films prepared; the surface roughness from the SEM images is in excellent agreement with the AFM results. The measured average grain sizes calculated from SEM images are shown as inset text on each figure, there is an observed increase in grain size as annealing temperature is increased. It is noted that the grain size of the 100 °C treated film appears to be in the region of 20 nm, in contrast to the data seem by HRTEM. We believe that the large grains observed by SEM contain clusters of the nanocrystalline ZnO, this is supported by the lack of XRD data from these films which would not be anticipated with a primary crystallite size of ~20 nm.

To investigate the behavior of these films as n-type thin films, bottom gate, bottom contact thin film transistors (TFTs) were prepared. Typical transfer curves and output characteristics measured under ambient conditions for several unencapsulated TFTs annealed between 100 – 450 °C are shown in **Figure 5a**. The as-cast film was too resistive and showed no on/off behavior, so is not displayed here. Between 100 – 450 °C, lower threshold voltages and higher channel current on/off ratios are observed as temperature increases, both indicative of improved electron transport. The turn-on voltage shifts towards more negative V_G with the increase in processing temperature which suggests that higher annealing temperatures lead to higher concentrations of free carriers in the channel. Enhanced electron transport with higher annealing temperature is also demonstrated from the calculated saturated field effect mobility, shown in **Figure 5b**. The as-cast film has very low mobility, 3.4×10^{-6} cm^2 $V^{-1}s^{-1}$, however for films at 100 – 450 °C, the mobility increases with the annealing temperature from 0.05 to 0.39 cm^2 $V^{-1}s^{-1}$.

The Fermi levels (E_F) of ZnO films on ITO substrates were calculated from the contact potential difference measured by Kelvin Probe in air, **Figure 5b**. Interestingly heating the as-cast films to 100 °C has no impact on E_F, which remains stable at -4.46 eV. Further heating to 200 °C leads to a slight reduction in E_F (-4.40 eV) and a significant shift to -4.63 eV is seen when annealing to 450 °C occurs. Native defects in ZnO (200 °C), including Zn interstitials and

oxygen vacancies, may be partially recovered when the films are annealed to 450 °C, evidenced by the enhanced crystallinity[35–37](confirmed by the XRD results); this may be origin of the differences in E_F observed. In addition, the work function shift measured by Kelvin probe is in excellent agreement with our XPS results: the binding energy position of the Zn−O (oxide) peak shifts towards higher binding energy upon annealing at 450 °C, **Supporting Figure 1**. This is indicative of a shift in the Fermi level position, which we would expect to manifest itself as a rigid shift of the core levels, and is indeed what we see in the Zn−O (oxide) environment of the O 1s[21]. The same trend is also observed from the Zn 2p spectra.

To assess the quality of the ZnO prepared as an n-type, electron transport layer (ETL) we incorporated the layers into inverted architecture OPVs with the general composition (layer thicknesses in parenthesis) of glass / ITO (140 nm) / ZnO (20 nm) / PCDTBT:$PC_{71}BM$ (100 nm) / MoO_x (10 nm) / Ag (100 nm), shown schematically in **Figure 6a**, alongside the relevant energy levels of the materials[43–46] in **Figure 6c** and molecular structure of the active layer materials **Figure 6b**. Both ZnO and the active layer were deposited from solution and the MoOx/Ag thermally evaporated. Representative current-voltage (J-V) characteristics are shown in **Figure 6d** where the ZnO processing temperatures is varied over the range 100 - 450 °C, also included is data for a control device prepared without ZnO. Statistical data for all devices prepared are summarized in **Table 2**. From these data it is clear that the ETL processing temperature is having a significant impact on device performance. Overall the best performing devices are observed at processing temperatures of 100 °C, where the champion device shows a PCE of 4.3 % and average open-circuit voltage (V_{OC}), short-circuit current (J_{SC}) and fill-factor (FF) of 0.89 V, 8.5 mA/cm^2 and 52 % respectively. The device characteristics over the temperature range 100 – 200 °C are comparable, and drop at 450 °C, consistent with our previous report[16] where the onset of crystallization in the ETL and a change in work function result in V_{OC} and FF losses. The dark J-V scans are shown in **Supporting Figure 3**. Improved hole blocking behavior at lower processing temperatures is observed under reverse bias. At low positive voltage, the difference of dark J-V characteristics highlights the reduced shunt resistance at ZnO (450 °C)[47]. Thus, our ETL fulfills the low temperature and charge selective transport criteria of such an interlayer.

Unsurprisingly poor performing devices are measured when no ETL is included in the device stack, suggesting that the necessity of ZnO ETL that enables device operation.

OLED devices were also fabricated, incorporating ZnO films as an electron injection layer (EIL). The results are shown in **Supporting Table 1,** while J-V-L data of representative devices for each temperature are presented in **Figure 7**. The trends observed in OPV devices are replicated here, with films annealed at 100 °C and 200 °C showing similar, more efficient behavior, and films treated at 450 °C showing higher performances than devices without any ETL but lower performances than the other two films. In particular, the higher turn on voltage shown when 450 °C ZnO was used confirmed what already speculated for OPV devices, that the deep work function affects the energy level alignment at the interface.

Conclusions

Here we successfully fabricate ZnO thin films processed using a remarkably simple solution processing and environmentally friendly route. By carrying out a range of complementary measurements, we demonstrate the importance of processing temperature on tuning structural, optical, compositional, surface morphological and electrical properties of the ZnO films. Using a combination of transmission electron microscopy and X-ray photoelectron spectroscopy, films prepared at temperatures as low as 100 °C are confirmed to e composed of ZnO nanoparticles that are remarkably free of unreacted precursor and water residues. The ZnO particle size increases with the annealing temperature, which is supported from the XRD, SEM and UV-Vis results. Significant changes on electron mobility and work function with ZnO processing temperature are shown by thin film transistor and Kelvin probe, respectively. To demonstrate the suitability of the films developed in device applications we have demonstrated their incorporation into OPV and OLED device platforms. Our objective was to develop a low temperature, environmentally friendly, facile solution processable charge selective interlayer for organic optoelectronic devices that had high optical transparency, good charge transport and smooth compact surface morphology. The ZnO films we have developed fulfill the criteria for OPV and OLED interlayers and for the future development of devices that are compatible with high throughput processing.

Experimental

Preparation

Indium tin oxide substrates (ITO, PsiOteC UK Ltd; 12–16 Ω/sq) were cleaned using ultrasonics and sequential washing in acetone, isopropanol and distilled water prior to being dried with compressed nitrogen gas followed by a 10 minutes UV-ozone clean (UVOCS).

Carbon-free aqueous zinc solutions were prepared by mixing zinc oxide powders (Sigma Aldrich) in ammonium hydroxide solution (5.0 M, Sigma Aldrich) as solvent to molar concentration of 0.1 M. Before spin coating, the solutions were filtered through a 0.45 μm filter. The spin coating of ZnO films was a 2000 rpm spinning for 30s with an acceleration rate of 1000 rpm/s. Four coatings were applied to achieve a compact layer. The films were preheated at a given temperature for 10 min on a hotplate after each coating. Some samples were also post annealed (Carbolite 5L RWF) at 450 ℃ for 1 hour under flowing air.

For OPV fabrication, PCDTBT:$PC_{71}BM$, 1:2, 18 mg/ml blend solution in chlorobenzene is spin-coated on the top of ZnO at 2500 rpm in order to achieve around 80-90nm. Finally, the deposition of the top electrode is done in the glovebox evaporator defining the patterned electrode by the shadow mask. The top electrode is 10nm of MoO_3 and 100 nm of Ag with evaporation rate of MoO_3 is 0.1-0.2 nm/s and Ag deposition rate of 0.8-1.0 nm/s.

For OLED fabrication, a green derivative of p-PPV obtained from Merck was dissolved in toluene in a 10 mg/ml concentration and stirred overnight at 60 °C. The solution was then spun dynamically at 1500 rpm for 40 s, which resulted in films 70 nm thick. The top electrode was deposited in the same way as that of OPV devices.

Characterization

XRD measurements were carried out using a Panalytical X'Pert Pro diffractometer (CuKα). The XRD instrumental broadening was confirmed as 0.09° by a single silicon substrate. The TEM cross-section was prepared using a Helios NanoLab DualBeam with sequential ion beam accelerating voltages of 30, 5 and 2 kV. TEM imaging was carried out using JEOL 2100F at 200 kV. Great care was taken to minimize the sample exposure to the electron beam.

FTIR (NICOLET iS10) was conducted in ATR mode (Attenuated Total Reflectance). Films for

XPS were deposited on ITO substrates. The XPS spectra were recorded on a Thermo Scientific K-Alpha+ X-ray photoelectron spectrometer operating at $2x10^{-9}$ mbar base pressure. This system incorporates a monochromated, microfocused Al Kα X-ray source (hv = 1486.6 eV) and a 180° double focusing hemispherical analyser with a 2D detector. The X-ray source was operated at 6 mA emission current and 12 kV anode bias. Data were collected at 200 eV pass energy for survey, 20 eV pass energy for core level using an X-ray spot size of 400 μm^2.

Optical transmission of ZnO films deposited on quartz substrates was measured using a single-beam UV–vis spectrometer (Agilent Technologies Cary 5000). Film morphology was assessed using (i) a Bruker Multimode Nanoscope AFM with image processing carried out using the Gwyddion software suite, and (ii) a LEO Gemini 1525 Field Emission Scanning Electron Microscope with the addition of a 5 nm layer of chromium.

Fraunhofer IPMS generation 5 substrates were used for all field effect measurements. The bottom gate n- doped silicon structures had a 230 nm thermally grown silicon dioxide dielectric layer with indium tin oxide (10 nm)/ gold (30 nm) source and drain bottom contact electrodes. Devices of 20 µm channel length and 10 000 µm channel width were characterized through the use of an Agilent 4155 C analyser. Work functions were calculated from the measured chemical potential using a Kelvin probe (KP technologies, SKP 5050) in air, calibrated to a freshly cleaved highly ordered pyrolytic graphite reference (work function = 4.47 eV)[48].

Device Testing

J–V characteristics were measured using a xenon lamp (1 Sun, AM 1.5 G) (Oriel Instruments) with a Keithley 2400 source meter. Power conversion efficiency (PCE), open circuit voltage (VOC), short circuit current density (JSC), fill factor (FF), series resistance (Rs) and shunt resistance (Rsh) are calculated using the J-V results. Rs and Rsh are extracted from the inverse slope of the J-V curve at I=0 and V=0, respectively. Generally, a minimum of 5 devices were applied for each set of processing conditions. OLED devices were characterized using a Kethley 2400 sourcemeter and a Minolta luminance meter, operated through a custom-written LabView script.

Acknowledgements

JZ and MAM thank Dr David J. Payne for fruitful discussions of the XPS data. JZ acknowledges

the National Key Research and Development Program of China (No. 2019YFA0705900) funded by MOST., the National Natural Science Foundation of China (No. 61804063), the National Science Foundation of Jilin Province (No. 20190201208JC), the Science and Technology Foundation of Department of Education, Jilin Province (Grant: JJKH20190136KJ) and the Open Foundation of State Key Laboratory of Inorganic Synthesis and Preparative Chemistry, Jilin University (Grant: 2019-24). MAM grateful for continued support through the EPSRC Centre for Doctoral Training in Plastic Electronics EP/L016702/1.

References

1 C. W. Tang, *Appl. Phys. Lett*., 1986, 48, 183–185.

2 C. W. Tang and S. A. VanSlyke, *Appl. Phys. Lett*., 1987, 51, 913–915.

3 S. H. Park, A. Roy, S. Beaupré, S. Cho, N. Coates, J. S. Moon, D. Moses, M. Leclerc, K. Lee and A. J. Heeger, *Nat. Photonics*, 2009, 3, 297–302.

4 K. M. Coakley and M. D. Mcgehee, *Chem. Mater*., 2004, 16, 4533–4542.

5 S. Reineke, F. Lindner, G. Schwartz, N. Seidler, K. Walzer, B. Lüssem and K. Leo, *Nature*, 2009, 459, 234–238.

6 K. Zilberberg, J. Meyer and T. Riedl, *J. Mater. Chem. C*, 2013, 1, 4796.

7 M. T. Greiner and Z. H. Lu, *NPG Asia Mater*., 2013, 5,55.

8 J. Meyer, S. Hamwi, M. Kröger, W. Kowalsky, T. Riedl and A. Kahn, *Adv. Mater*., 2012, 24, 5408–5427.

9 (a) A. B. Djurišić, X. Liu and Y. H. Leung, *Phys. status solidi - Rapid Res. Lett*., 2014, 8, 123–132. (b) R. M. Hewlett and M. A. McLachlan, *Adv. Mater.*, 2016, 28, 3893–3921.

10 U. Özgür, Y. I. Alivov, C. Liu, A. Teke, M. a. Reshchikov, S. Doğan, V. Avrutin, S. J. Cho and H. Morkoç, J. *Appl. Phys*., 2005, 98, 41301.

11 J. M. Downing, M. P. Ryan and M. A. McLachlan, *Thin Solid Films*., 2013, 539, 18–22.

12 J. C. D. Faria, A. J. Campbell and M. A. McLachlan, *Adv. Funct. Mater*., 2015, 25, 4657–4663.

13 J. B. Franklin, J. M. Downing, F. Giuliani, M. P. Ryan and M. A. McLachlan, *Adv. Energy Mater*., 2012, 2, 528–531.

14 R. Maller, Y. Porte, H. N. Alshareef and M. A. McLachlan, *J. Mater. Chem. C*, 2016, 4,

5953–5961.

15 Y. Sun, J. H. Seo, C. J. Takacs, J. Seifter and A. J. Heeger, *Adv. Mater*., 2011, 23, 1679–1683.

16 J. Zhang, J. C. D. Faria, M. Morbidoni, Y. Porte, C. H. Burgess, K. Harrabi and M. A. McLachlan, *Adv. Electron. Mater*., 2016, 2, 1600008.

17 S. K. Hau, H. L. Yip, N. S. Baek, J. Zou, K. O'Malley and A. K. Y. Jen, *Appl. Phys. Lett*., 2008, 92, 1–4.

18 H. Aqoma, S. Park, H.Y. Park, W.T. Hadmojo, S.H. Oh, S. Nho, D.H. Kim, J. Seo, S. Park, D.Y. Ryu, *Adv. Sci*., 2018, 5, 1700858.

19 M.A. Mahmud, N.K. Elumalai, M.B. Upama, D. Wang, V.R. Goncales, M. Wright, C. Xu, F. Haque, A. Uddin, *J. Power Sources*.,2018, 383, 59-71.

20 R. M. Hewlett and M. A. McLachlan, *Adv. Mater.*, 2016, **28**, 3893–3921.

21 J. Zhang, M. Morbidoni, C.H. Burgess, J. Wu, T. Du, K. Harrabi, D. J. Payne, J. R. Durrant, M.A. McLachlan, *Cryst. Growth Des*., 2017, 17, 6559-6564.

22 Z. E. Allouni, M. R. Cimpan, P. J. Høl, T. Skodvin and N. R. Gjerdet, *Colloids Surf., B*., 2009, 68, 83–87.

23 M. R. Arefi and S. Rezaei-Zarchi, *Int. J. Mol. Sci*., 2012, 13, 4340–4350.

24 S. Meyers and J. Anderson, *J. Am. Chem. Soc*., 2008, 17603–17609.

25 X. Xu, Q. Cui, Y. Jin and X. Guo, *Appl. Phys. Lett*., 2012, 101, 222114.

26 S. Y. Park, B. J. Kim, K. Kim, M. S. Kang, K. H. Lim, T. Il Lee, J. M. Myoung, H. K. Baik, J. H. Cho and Y. S. Kim, *Adv. Mater*., 2012, 24, 834–8.

27 Y. H. Lin, H. Faber, K. Zhao, Q. Wang, A. Amassian, M. A. McLachlan and T. D. Anthopoulos, *Adv. Mater*., 2013, 25, 4340–6.

28 Y. H. Lin, S. R. Thomas, H. Faber, R. Li, M. A. McLachlan, P. A. Patsalas and T. D. Anthopoulos, *Adv. Electron. Mater*., 2016, 2, 1–11.

29 K. Song, J. Noh, T. Jun, Y. Jung, H. Y. Kang and J. Moon, *Adv. Mater*., 2010, 22, 4308–4312.

30 S. Bai, Z. Wu, X. Xu, Y. Jin, B. Sun, X. Guo, S. He, X. Wang, Z. Ye, H. Wei, X. Han and W. Ma, *Appl. Phys. Lett*., 2012, 100, 203906.

31 Y. Chen, Z. Hu, Z. Zhong, W. Shi, J. Peng, J. Wang and Y. Cao, *J. Phys. Chem. C*, 2014, 118,

21819–21825.

32 D. Chen, C. Zhang, Z. Wang, J. Zhang, S. Tang, W. Wei, L. Sun and Y. Hao, *Appl. Phys. Lett*., 2014, 104, 1–5.

33 W. Wei, C. Zhang, D. Chen, Z. Wang, C. Zhu, J. Zhang, X. Lu and Y. Hao, *ACS. Appl. Mater. Interfaces*., 2013, 5, 13318–13324.

34 Y. Ka, E. Lee, S. Y. Park, J. Seo, D. G. Kwon, H. H. Lee, Y. Park, Y. S. Kim and C. Kim, *Org. Electron*., 2013, 14, 100–104.

35 K. D. G. I. Jayawardena, S. Li, L. F. Sam, C. T. G. Smith, M. J. Beliatis, K. K. Gandhi, M. R. R. Prabhath, T. R. Pozegic, S. Chen, X. Xu, G. D. M. R. Dabera, L. J. Rozanski, R. A. Sporea, C. A. Mills, X. Guo and S. R. P. Silva, *Nanoscale*., 2015, 7, 14241–14247.

36 J.Q. Zhang, M. Morbidoni, K.K. Huang, S.H. Feng, M.A. Mclachian, Inorganic. *Chemistry. Frontiers*., 2018, 5, 84-89.

37 J. G. Lu, Z. Z. Ye, Y. Z. Zhang, Q. L. Liang, S. Fujita and Z. L. Wang, *Appl. Phys. Lett*., 2006, 89, 4–6.

38 H. M. Cheng, K. F. Lin, H. C. Hsu and W. F. Hsieh, *Appl. Phys. Lett*., 2006, 88, 261909.

39 B. A. MacLeod, B. J. Tremolet de Villers, P. Schulz, P. F. Ndione, H. Kim, A. J. Giordano, K. Zhu, S. R. Marder, S. Graham, J. J. Berry, A. Kahn and D. C. Olson, *Energy Environ. Sci*., 2015, 8, 592–601.

40 C. Jiang, R. R. Lunt, P. M. Duxbury and P. P. Zhang, *RSC Adv*., 2014, 4, 3604.

41 P. Nunes, E. Fortunato and R. Martins, *Thin Solid Films*., 2001, 383, 277–280.

42 Y. Natsume and H. Sakata, *Thin Solid Films*., 2000, 372, 30–36.

43 J. Liu, S. Shao, G. Fang, B. Meng, Z. Xie and L. Wang, *Adv. Mater*., 2012, 24, 2774–9.

44 S. H. Park, A. Roy, S. Beaupré, S. Cho, N. Coates, J. S. Moon, D. Moses, M. Leclerc, K. Lee and A. J. Heeger, *Nat. Photonics.*, 2009, 3, 297–302.

45 X. Ouyang, R. Peng, L. Ai, X. Zhang and Z. Ge, *Nat. Photonics.*, 2015, 9, 520–524.

46 M. Kröger, S. Hamwi, J. Meyer, T. Riedl, W. Kowalsky and A. Kahn, *Org. Electron*., 2009, 10, 932–938.

47 J. D. Servaites, M. A. Ratner and T. J. Marks, *Energy Environ. Sci*., 2011, 4, 4410.

48 W. N. Hansen and G. J. Hansen, *Surf. Sci*., 2001, 481, 172–184.

Figure Captions

Figure 1 a) X-ray diffraction patterns for ZnO thin films prepared at the temperatures indicated, the data is consistent with the reference pattern (ICSD 01-079-0205), b) HRTEM image showing the 100 ℃ annealed ZnO layer deposited on ITO substrate (lower dark area), indicating the nanocrystalline nature of the films. A selection of lattice spacings and corresponding wurtzite ZnO planes are annotated and the inset shows a fast Fourier transform (FFT). c) UV-vis transmittance spectra showing highly transparent films in visible region are prepared at all temperatures and the inset shows a optical picture of a ZnO (200 °C) coated glass ITO substrate, d) calculated Tauc plots (direct band gap) showing the optical band gap of ZnO decreases with the processing temperature increase.

Figure 2 ZnO XPS spectra of O 1s, with different processing temperatures.

Figure 3 Representative AFM images of ITO substrate and ZnO films deposited on ITO substrates, a well-defined granular structure is observed on ZnO films at 100 – 450 °C. Insets show the RMS roughness of the film surfaces.

Figure 4 SEM images of ZnO films, as-prepared film showing 'cloudy' surface whereas excellent spatial uniformity for all other temperatures. Insets show the granular sizes measured from the SEM images.

Figure 5 a) Transfer curves of bottom gate, bottom contact thin film transistors (TFTs) of ZnO films prepared at 100 – 450 °C with V_D = 35 V, b) Field effect mobilities of ZnO films calculated from transfer curves in the saturation region, with inset showing work functions of ZnO prepared on ITO substrates, measured by Kelvin probe.

Figure 6 a) Schematic illustration of organic solar cells with inverted device architecture, b) Molecular structure of electron donor (PCDTBT) and acceptor ($PC_{71}BM$) active layer materials, c) Energy level diagram of devices and d) Representative J-V curves for devices prepared using ZnO electron transport layers (ETLs) deposited at the temperatures indicated.

Figure 7 Representative J-L-V curves for OLED devices prepared using ZnO electron transport layers (ETLs) deposited at the temperatures indicated.

Table 1 ZnO grain sizes calculated from XRD data,

Table 2 Statistical data of OPV device parameters measured over the range of ETL processing temperatures.

Supporting Figure 1 XPS spectra of ZnO with different processing temperatures: a) C 1s signal, used to align the B.E. positions of all spectra, b) N 1s signal, no nitrogen signal is detected even at 100 °C processed ZnO surface c) Zn 2p and d) O 1s (O-Zn), indicating the E_F shift with ZnO annealing temperatures.

Supporting Figure 2 Large area SEM images of ZnO films showing fully covered and compact surface morphologies for films with all processing temperatures.

Supporting Figure 3 Representative dark J-V curves for devices prepared using ZnO electron transport layers (ETLs) deposited at the temperatures indicated.

Supporting Table 1 Performance metrics of OLED devices measured over the range of ETL processing temperatures.

FIGURE 1

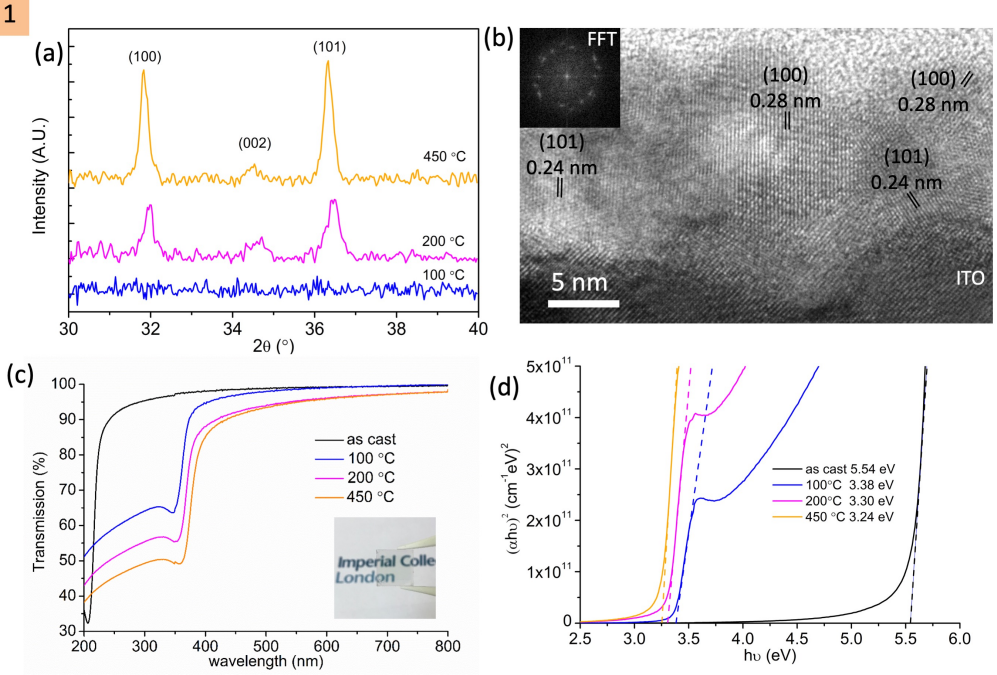
(a)
(100)
(101)
(002)
450 °C
200 °C
100 °C
Intensity (A.U.)
2θ (°)
(b)
FFT
(100)
0.28 nm
(100) //
0.28 nm
(101)
0.24 nm
(101)
0.24 nm
5 nm
ITO
(c)
as cast
100 °C
200 °C
450 °C
Transmission (%)
wavelength (nm)
(d)
as cast 5.54 eV
100°C 3.38 eV
200°C 3.30 eV
450 °C 3.24 eV
(αhυ)² (cm⁻¹eV)²
hυ (eV)

FIGURE 2

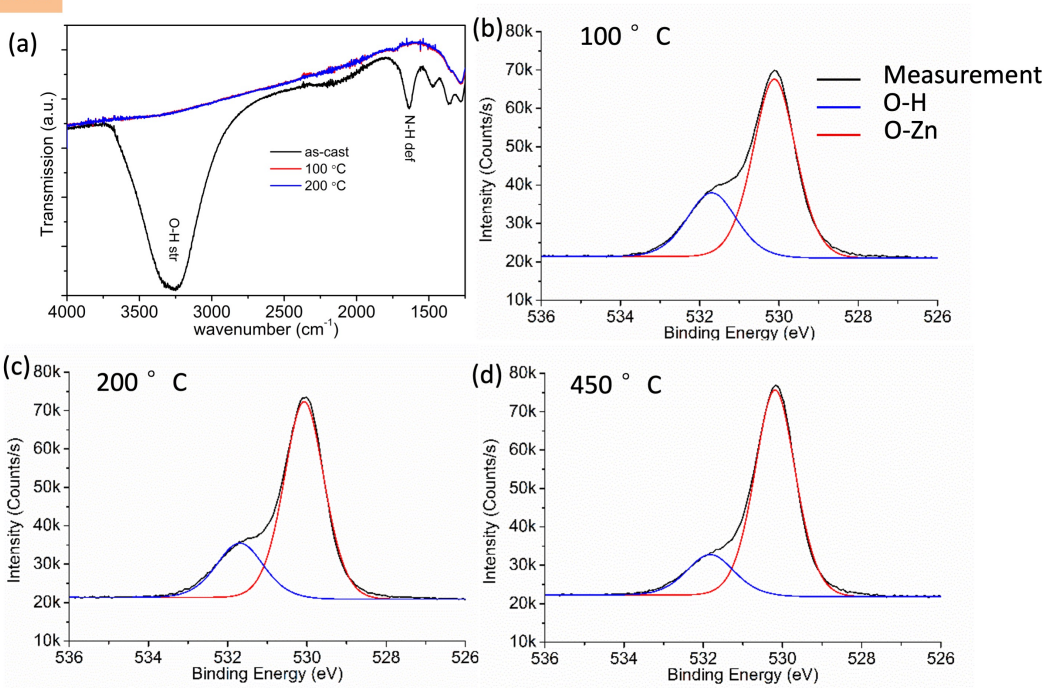
(a)
Transmission (a.u.)
wavenumber (cm-1)
as-cast
100 °C
200 °C
O-H str
N-H def
(b)
100 ° C
Measurement
O-H
O-Zn
Intensity (Counts/s)
Binding Energy (eV)
(c)
200 ° C
Intensity (Counts/s)
Binding Energy (eV)
(d)
450 ° C
Intensity (Counts/s)
Binding Energy (eV)

FIGURE 3

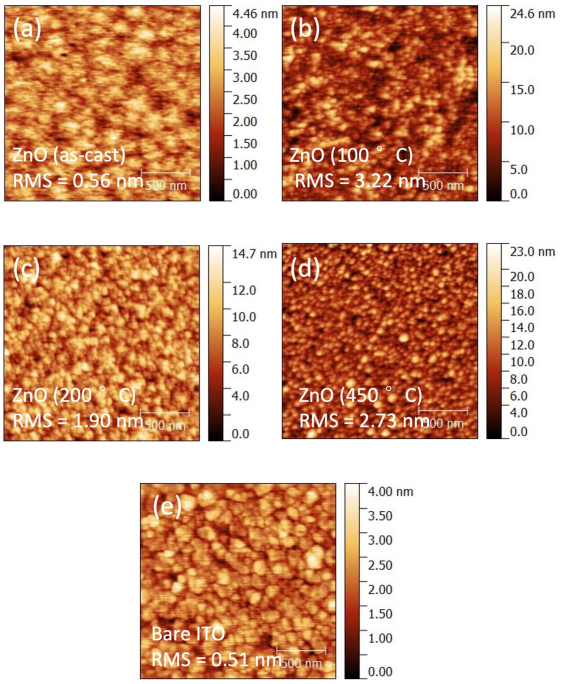
(a)
ZnO (as-cast)
RMS = 0.56 nm
500 nm
4.46 nm
4.00
3.50
3.00
2.50
2.00
1.50
1.00
0.00
(b)
ZnO (100 ° C)
RMS = 3.22 nm
500 nm
24.6 nm
20.0
15.0
10.0
5.0
0.0
(c)
ZnO (200 ° C)
RMS = 1.90 nm
500 nm
14.7 nm
12.0
10.0
8.0
6.0
4.0
0.0
(d)
ZnO (450 ° C)
RMS = 2.73 nm
500 nm
23.0 nm
20.0
18.0
16.0
14.0
12.0
10.0
8.0
6.0
4.0
0.0
(e)
Bare ITO
RMS = 0.51 nm
500 nm
4.00 nm
3.50
3.00
2.50
2.00
1.50
1.00
0.00

FIGURE 4

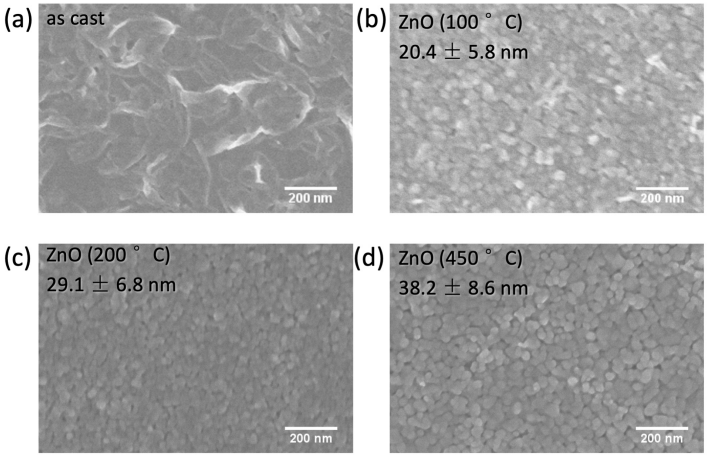
(a)
as cast
200 nm
(b)
ZnO (100 ° C)
20.4 ± 5.8 nm
200 nm
(c)
ZnO (200 ° C)
29.1 ± 6.8 nm
200 nm
(d)
ZnO (450 ° C)
38.2 ± 8.6 nm
200 nm

FIGURE 5

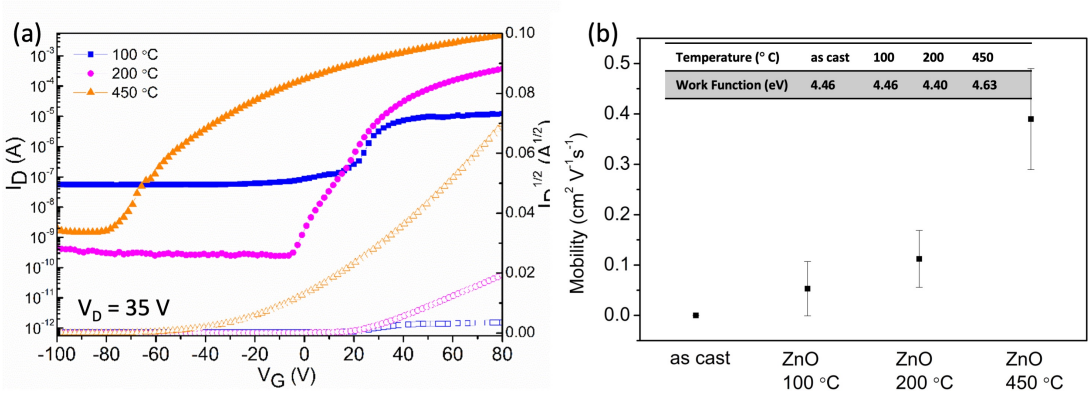
(a)
100 °C
200 °C
450 °C
V_D = 35 V
I_D (A)
$I_D^{1/2}$ ($A^{1/2}$)
V_G (V)
(b)
Temperature (° C) as cast 100 200 450
Work Function (eV) 4.46 4.46 4.40 4.63
Mobility ($cm^2 V^{-1} s^{-1}$)
as cast
ZnO 100 °C
ZnO 200 °C
ZnO 450 °C

FIGURE 6

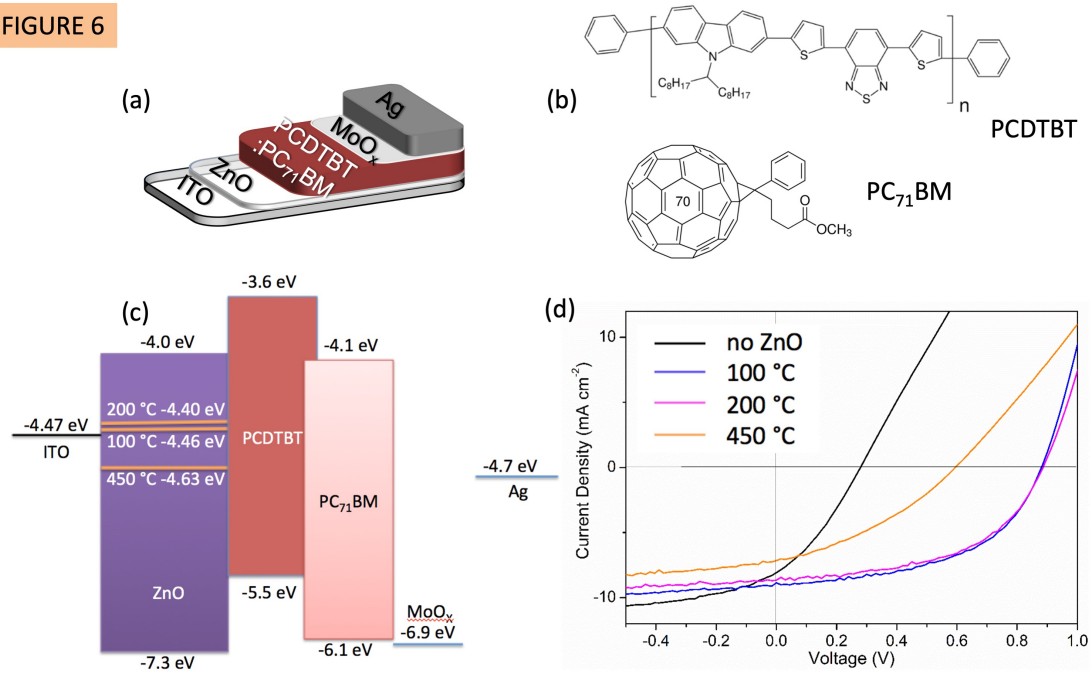
(a)
Ag
MoOx
PCDTBT
:PC71BM
ZnO
ITO
(b)
PCDTBT
PC71BM
(c)
-3.6 eV
-4.0 eV
-4.1 eV
200 °C -4.40 eV
-4.47 eV
100 °C -4.46 eV
PCDTBT
450 °C -4.63 eV
PC71BM
ITO
ZnO
-5.5 eV
MoOx
-6.9 eV
-6.1 eV
-7.3 eV
-4.7 eV
Ag
(d)
no ZnO
100 °C
200 °C
450 °C
Current Density (mA cm-2)
Voltage (V)

FIGURE 7

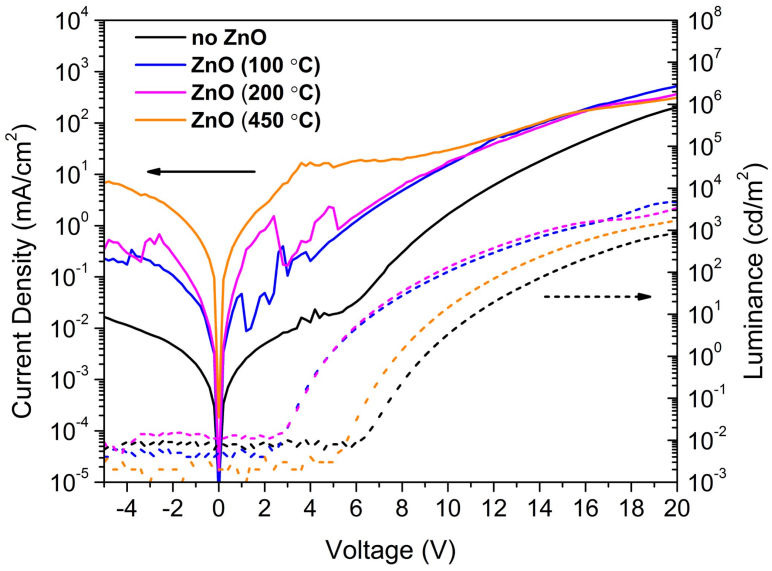
no ZnO
ZnO (100 °C)
ZnO (200 °C)
ZnO (450 °C)
Current Density (mA/cm^2)
Luminance (cd/m^2)
Voltage (V)
10^4
10^3
10^2
10^1
10^0
10^{-1}
10^{-2}
10^{-3}
10^{-4}
10^{-5}
10^8
10^7
10^6
10^5
10^4
10^3
10^2
10^1
10^0
10^{-1}
10^{-2}
10^{-3}
-4 -2 0 2 4 6 8 10 12 14 16 18 20

TABLE 1

	100 ˚C	200 ˚C	450 ˚C
$d_{(101)}$ (nm)	N/A	31.0	52.3
$d_{(100)}$ (nm)	N/A	51.6	59.0

TABLE 2

Sample	V_{oc} (V)	J_{sc} (mA/cm^2)	FF (%)	PCE (%)	Rs (Ω cm^2)	Rsh (Ω cm^2)
no ZnO	0.242 ± 0.049	6.61 ± 1.00	31.6 ± 2.7	0.52 ± 0.16	26.2 ± 3.2	67.7 ± 27.7
ZnO (100 ˚C)	0.886 ± 0.003	8.47 ± 0.72	52.1 ± 1.3	3.97 ± 0.28	18.5 ± 2.4	569.9 ± 39.0
ZnO (200 ˚C)	0.883 ± 0.004	8.41 ± 0.37	51.1 ± 0.6	3.86 ± 0.22	20.3 ± 0.8	607.3 ± 163.6
ZnO (450 ˚C)	0.591 ± 0.011	6.65 ± 0.61	36.1 ± 1.4	1.43 ± 0.08	43.1 ± 2.4	255.5 ± 51.1

SUPPORTING FIGURE 1

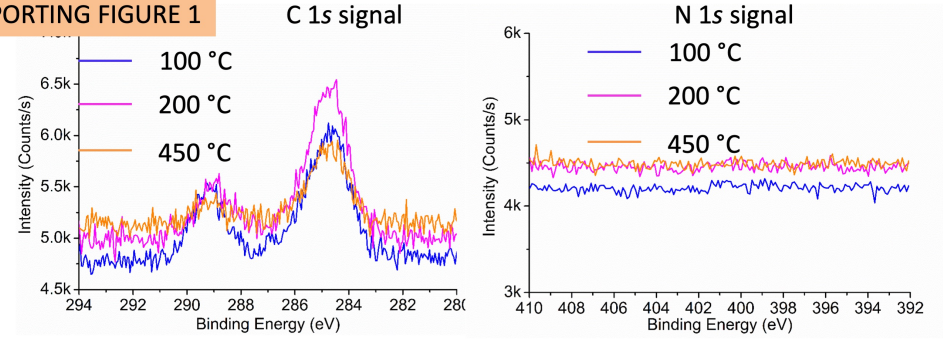

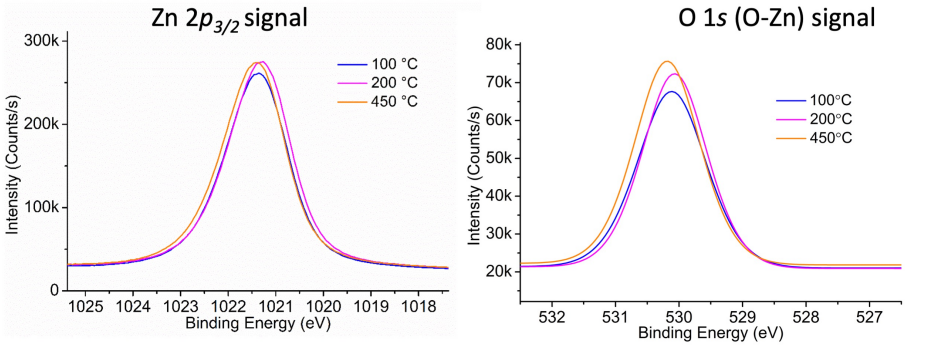

SUPPORTING FIGURE 2

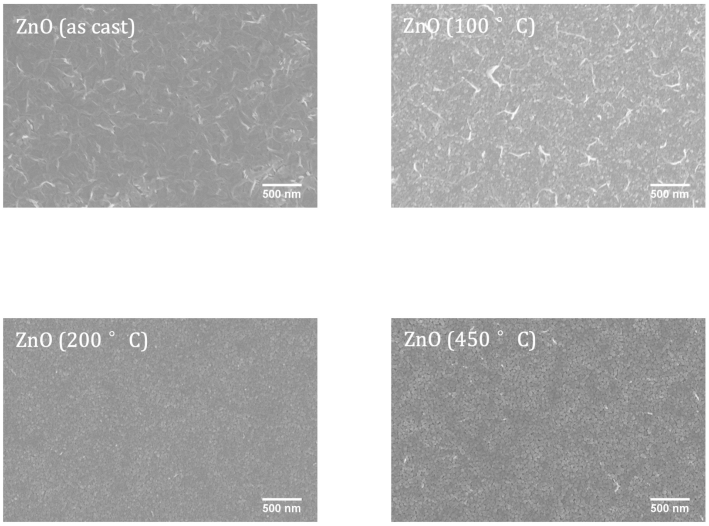

SUPPORTING FIGURE 3

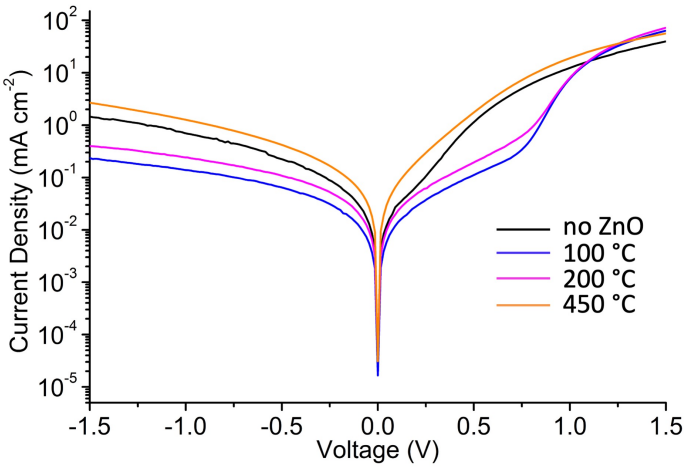

SUPPORTING TABLE 1

Sample	Maximum current efficiency (Cd/A)	Voltage at maximum current efficiency (V)	Power efficiency at maximum current efficiency (Lm/W)	Luminance at maximum current efficiency (Cd/m^2)	Current density at maximum current efficiency (mA/cm^2)	Turn-on voltage (V)
No ZnO	0.45	17.8	0.08	470	105.21	6.4
ZnO (100 °C)	1.00	19.0	0.17	4160	414.00	2.6
ZnO (200 °C)	1.03	13.2	0.25	640	62.10	2.6
ZnO (450 °C)	0.67	21.4	0.10	2970	443.00	5.4